

# Brain Mapping

## Introduction

Activity-dependent hemodynamic signals are being extensively used for functional brain imaging, including positron emission tomography (PET) ([Fox and Raichle, 1985](#)), optical imaging of intrinsic signals ([Grinvald et al., 1986](#)), and functional magnetic resonance imaging (fMRI) ([Ogawa et al. 1990](#); [Ogawa et al. 1992](#); [Bandettini et al. 1992](#) and [Kwong et al. 1992](#)). All these techniques rely on the seminal findings of [Roy and Sherrington \(1890\)](#) regarding the coupling between changes in electrical activity and the various components of the microcirculation's response. Evidently, the spatial scale at which any given hemodynamic signal is regulated by local electrical activity sets the upper limit for the spatial resolution achievable, independently of the technique used. Yet, for some of the hemodynamic responses, a detailed characterization of their degree of spatial localization is still missing.

When aiming for functional imaging at the columnar level, the contribution of the global part of the responses, resulting from hemodynamic activity regulated at coarse spatial scale, is to be minimized with respect to the contribution of the responses' local part, which closely colocalizes with electrical activity. "Differential" imaging achieves this goal by comparing the activity patterns elicited by two appropriately chosen stimuli, e.g., using subtraction or division ([Bonhoeffer and Grinvald, 1996](#)). In the resulting differential map, the hemodynamic responses' global part, which is mostly (although not completely) stimulus-*nonspecific*, is nearly eliminated. Differential imaging, however, requires the two compared stimuli to be "orthogonal," i.e., known to activate spatially nonoverlapping neuronal populations; otherwise, the activity patterns attributed to the stimuli are wrongly estimated. Unfortunately, such a priori knowledge about the expected activation by the stimuli is not available in the general case, and when studying higher brain areas, such orthogonal stimuli might not even exist. Alternatively, the hemodynamic activity patterns elicited by a given stimulus can be compared to those recorded in absence of stimulation ("blank"), averaged over many trials to get rid of eventual contribution of large "ongoing" activity ([Arieli et al., 1996](#)). Although this procedure, termed "single-condition" mapping, can overcome the shortcomings of differential imaging, here, the hemodynamic responses contribute as a whole to the obtained map, including the part that does not colocalize with electrical activity. To optimally choose a particular signal for high-resolution imaging, it is thus important to carefully evaluate the global and local part of the contributing hemodynamic responses, especially when single-condition imaging is required.

Since increasing oxygen extraction by the electrically active neurons or the surrounding glia ([Vanzetta and Grinvald 1999](#) and [Ances et al. 2001](#)) depends on local electrical activity ([Thompson et al., 2003](#)), naturally, an increase in the conversion rate of oxy-hemoglobin (HbO<sub>2</sub>) into deoxy-hemoglobin (Hbr) provides a hemodynamic signal component that colocalizes with areas of electrical activity at fine spatial scale. Therefore, the "initial dip," i.e., the initial increase in [Hbr] (amount of Hbr per sampled tissue-volume unit), observed just after stimulus onset with optical imaging of intrinsic

signals ([Frostig et al., 1990](#)), imaging spectroscopy in anesthetized ([Malonek and Grinvald 1996](#) and [Mayhew et al. 1999](#)) and awake preparations ([Shtoyerman et al. 2000](#) and [Martin et al. 2002](#)), and high-field BOLD-fMRI ([Ernst and Hennig 1994](#); [Menon et al. 1995](#); [Hu et al. 1997](#); [Logothetis et al. 1999](#) and [Kim et al. 2000](#)) should contain a large local component. Indeed, using the initial dip, functional single-condition maps at columnar resolution were obtained by optical imaging ([Frostig et al. 1990](#); [Grinvald et al. 2000](#); [Shoham and Grinvald 2001](#) and [Masino 2003](#)) and fMRI ([Kim et al. 2000](#) and [Duong et al. 2001](#)). Since, however, the signal from the initial dip is small as compared to the later positive BOLD and because confirmation of single-condition fMRI maps by established independent measurements has not been reported, the best way to achieve single-condition maps with fMRI remains highly controversial ([Logothetis 2000](#); [Kim 2000](#) and [Duong et al. 2001](#)).

Of great interest has been the level of spatial regulation of activity-dependent cerebral blood volume (CBV) and blood flow (CBF) changes. Previous optical imaging and imaging spectroscopy work in the visual cortex of cats and monkeys ([Frostig et al. 1990](#); [Malonek and Grinvald 1996](#); [Shtoyerman et al. 2000](#) and [Vanzetta and Grinvald 2001](#)) reported that CBV changes colocalize with the electrically active columns to a much lower extent than the [Hbr] increase during the initial dip, and functional single-condition maps were obtained by imaging the oximetric signal but not by imaging CBV changes. Still, some part of the CBV signal is local. Indeed, high-quality functional CBV maps are readily obtained upon differential optical imaging ([Frostig et al., 1990](#)). Furthermore, [Menon et al. \(1997\)](#), [Goodyear and Menon \(2001\)](#), and [Cheng et al. \(2001\)](#) obtained differential maps of ocular dominance columns in humans, exploiting the hyperoxic phase of the BOLD fMRI signal, dominated by the CBV and CBF responses. However, it remains unresolved whether this local part of the CBV signal can be identified with the response of a precise microvascular compartment and whether, if selectively imaged, this component would allow obtaining single-condition maps eventually comparable to those obtained by using the initial dip.

We address these questions by comparing the quality of various single-condition maps based on activity-evoked changes in oximetry and CBV, using high-resolution optical imaging of intrinsic signals. Unlike fMRI, these allow straightforward identification of the vascular versus the parenchymal signal. Whereas a recent report ([Sheth et al., 2004](#)) addressed this issue in the anesthetized rat barrel cortex, here we preferred to use the awake primate model to make the conclusions more relevant for human functional brain mapping. Removing surface vascular activity by postprocessing, we prove the existence of a highly local component of the CBV signal. We attribute this component to the capillary CBV response. Although the best functional maps were obtained by imaging the oximetric changes during the initial dip, the results suggest that single-condition functional maps at columnar resolution can be obtained also by using the CBV signal, provided that the capillary component of the CBV response is selectively imaged.

## Results

### Differential Imaging

To compare oximetric functional maps with CBV maps, a sequence of cortical images was taken while a monkey was viewing a stimulus either with the right or with the left eye. The cortex was illuminated either at 605 nm, emphasizing oximetric changes and thus providing "oximetric maps," or at 570 nm, an isosbestic wavelength for Hbr and HbO<sub>2</sub> and thus sensitive mainly to changes in CBV, providing "blood volume maps" (Frostig et al., 1990). The differential maps shown in [Figures 1B and 1C](#) were obtained by dividing the images taken during contralateral stimulation by those taken during ipsilateral stimulation, averaged over the time interval yielding the best functional maps: the initial dip for 605 nm and the time from response onset until the end of data acquisition for 570 nm (8.5 s). As expected from the study of [Frostig et al. \(1990\)](#), functional maps were obtained at both wavelengths. Still, the activity patterns obtained from the CBV maps ([Figure 1C](#)) were partially distorted with respect to the patterns obtained from the oximetric differential maps ([Figure 1B](#)). In the following, we refer to those maps as the "gold standard," since they have been shown to faithfully reflect the underlying functional architecture in numerous previous studies combining optical imaging with electrophysiology and histology ([Bonhoeffer and Grinvald 1991](#); [Shmuel and Grinvald 1996](#); [Wang et al. 1996](#); [Weliky et al. 1996](#); [Bosking et al. 1997](#) and [Shoham et al. 1997](#)). To quantify the similarity of the functional maps obtained at the two wavelengths, their correlation coefficient,  $R$ , was calculated. As opposed to the maps displayed in the figures, for this calculation, all maps were spatially low-pass filtered for the purpose of avoiding correlation artifacts due to the presence of—albeit weak—blood vessel patterns in addition to the functional patches. We found  $R = 0.53$ , indicating that the two maps in [Figures 1B and 1C](#) strongly resembled each other. The close similarity between the two differential maps is evident also in another monkey in which ocular dominance columns were imaged over a larger area. ([Figures 1E–1G](#)).

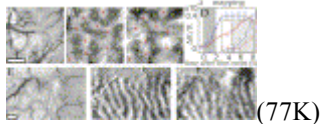


Figure 1. Differential Maps and Mapping Signal Time Courses (A) Cortical vasculature (image taken at 570 nm). (B and C) Differential maps, obtained upon imaging at 605 nm (B) for the time of the initial dip, and at 570 nm (C), from stimulus onset until end of data acquisition (8.5 s). Maps' amplitudes (clipping range): 0.14% (B) and 0.46% (C). To facilitate comparisons of functional maps, red and green crosses, herein and elsewhere, mark bright and dark functional patches, obtained from the 605 nm differential map (B). (D) Mapping signal time courses. Blue: 605 nm. Red: 570 nm. The larger 570 nm signal was downsampled by a factor of 4 for display purposes. Error bars: SEM of seven imaging sessions, performed on two monkeys. Throughout the paper, the shaded area marks the stimulus duration. Inset: expanded view of the first 2 s of the response. (E–G) Same as in (A), (B), and (C), obtained in a second monkey, using low magnification. At the top, the image includes a small part of V2. Clipping range: 0.16% (F) and 0.9% (G). Scale bars: 1 mm. Note that the blood volume maps are similar but not identical to the oximetric ones; e.g., the "C-shaped" black patch seen in (B) at half-height on the far right of the image is missing in (C). Also, the blood volume map (G) shows a white and a black patch of vascular origin right on the V1/V2 border (top right), which is absent in the corresponding oximetric map (F).

To quantify the time course of the differential functional maps we calculated the "mapping signal," defined as the difference in activation amplitude between ipsi- and

contralateral stimuli in a cortical location with ipsilateral preference or vice versa ([Grinvald et al. 1986](#); [Frostig et al. 1990](#) and [Malonek and Grinvald 1996](#)). To increase the signal-to-noise ratio (SNR), the mapping signal was averaged over all centers of the ocular dominance columns. The resulting traces are shown in [Figure 1D](#). The fast increase and the characteristic plateau of the 605 nm mapping signal time course as opposed to the monotonous increase of the CBV mapping signal underscores the different physiological processes underlying the two signals.

### Time Course of the Single-Condition Maps

Single-condition maps were obtained by dividing images recorded during a stimulus by the images recorded during a blank condition. The time course is shown in [Figure 2](#) at a time resolution of 950 ms.

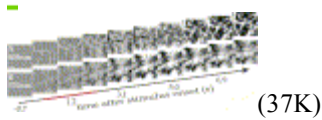


Figure 2. Time Development of Single-Condition OD Maps Obtained in Interlaced Imaging Sessions at 605 and 570 nm (A) 605 nm; (B) 570 nm. For each time series, the spatial pattern prior to stimulus onset was subtracted from all frames. To show the time development of the maps' amplitudes, the same clipping range was used for displaying every frame in the time series, after subtraction of its mean gray level. Clipping range: 0.2% (A) and 1.4% (B). Scale BAR = 1 mm. Here and in Figures 3 and 6, the red bar marks the time during which the stimulus was on.

Larger numbers of vessels were activated at 570 than at 605 nm, not colocalizing with the functional architecture. These vascular responses exhibited much higher reproducibility and stimulus specificity in blood volume maps than in oximetric maps obtained during the period of the initial dip. This was especially apparent for small vessels (30–100  $\mu\text{m}$ ), giving rise to distortions even in differential CBV maps (e.g., [Figure 1F](#) versus [Figure 1G](#)), indicating that the nonlocal, yet stimulus-specific, part of the macrovasculature's CBV response is larger than that of the oximetric changes during the initial dip. Thus, reproducibility of maps obtained by indirect measurements is not a sufficient criterion for their functional character, underscoring the importance of carefully evaluating the local versus global components' amplitudes in a given signal used for functional imaging.

Clear single-condition ocular dominance (OD) patches were observed only at the oximetric wavelength ([Figure 2A](#)). The definition of the functional maps at 605 nm was best ( $R = 0.72$ ) during the initial dip (first 3.5 s). At later times, functional patches were seen together only with prominent vascular activation patterns of much larger amplitude, and therefore the correlation with the gold standard was small ( $R = 0.09$ ). The "late patches" were seen better by redisplaying the data in [Figure 2A](#) after clipping each frame individually to  $\pm 2$  standard deviations in the frame's pixels' gray level ([Figure 3A](#)), thus matching the grayscale to each data-frame's individual dynamic range. Indeed, due to the high spatial resolution and the focus on the vasculature, the functional or vascular origin of the signals could be visually identified in these experiments. Depending on the particular experimental session and monkey, late single-condition patches could or could

not be seen. In cases in which the global brightening of the cortex at 605 nm was large, indicating a large CBF response and thus a large macrovascular signal, the identification of such late functional patches was particularly difficult or even impossible. Whenever late functional patches could be seen, they were observed together with prominent vascular activation of vessels even smaller than  $50 \mu\text{m}$ .

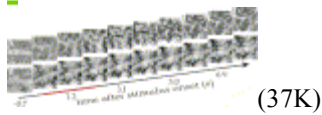


Figure 3. Time Development of the Single-Condition OD Maps(A) 605 nm; (B) 570 nm. Same data as in [Figure 2](#), but displayed such as to enhance spatial patterns at each point in time. After subtraction of the spatial pattern prior to stimulus onset, each frame was clipped individually to  $\pm 2$  standard deviations from its mean gray level, calculated from the gray level distribution of all of its pixels. Scale BAR = 1 mm.

In contrast with the results observed for the oximetric maps, no OD patches could be observed in the single-condition maps obtained from CBV changes ( $R \sim 0.22$ ) imaged at 570 nm ([Figure 2](#) and [Figure 3](#)). Here, images of extensive surface vasculature obscured any traces of functional architecture, even at the high magnification used. These activation patterns reflected the large vascular component of the CBV response, completely masking the local part of the CBV responses.

### Separating Functional and Vascular Patterns in Single-Condition Maps

To increase the SNR, the single-condition maps were integrated over time, separating the period of the initial dip (the first  $\sim 3.5$  s after stimulus onset; [Figure 5B](#)), "early," from the later period, "late" ([Figure 4](#), top).

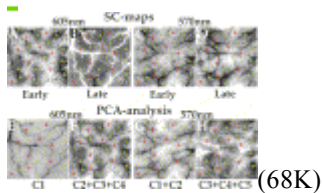


Figure 4. Separation of Functional from Vascular Components in Single-Condition MapsTop: Spatial patterns in single-condition maps at 605 and 570 nm, integrated over the initial dip and over the late phase of the hemodynamic response. (A) 605 nm, averaged from 0 to 3.8 s, clipping range: 0.06%; (B) 605 nm, averaged from 5.7 to 8.55 s, clipping range: 0.4%; (C and D) 570 nm, averaged over same times as (A) and (B), clipping range: 0.55% and 2.74%, respectively. Bottom: Vascular maps (E and G) and functional maps (F and H), obtained from principal component analysis (PCA). Functional maps were obtained by decomposing the single-condition maps time courses at 605 and 570 nm into principal components and summing separately the eigenvectors displaying the most evident vascular patterns (C1 and C1+C2, respectively, clipping range: 2.7%) and the eigenvectors displaying the most evident functional patterns (C2+C3+C4 and C3+C4+C5, respectively, clipping range: 2.6%). For both wavelengths, the functional patterns obtained by PCA reproduced the OD patterns. Note that the separation is not complete. In particular, the functional image at 570 nm (H) is contaminated by vascular activation. Scale BAR = 1 mm.

At 605 nm, the clearest functional patches were obtained at early times ([Figure 4A](#)). Since the focus on the vasculature and the high magnification allowed a clear identification of vascular elements and functional architecture, a large part of the functional patches could be identified also during the subsequent hyperoxygenation phase ([Figure 4B](#)). The dominant features in this later image, however, were high-amplitude vascular signals. During the hyperoxygenation phase, the functional architecture thus easily becomes unrecognizable—especially at low spatial resolution—unless the vascular patterns are known a priori or can be rejected according to morphological criteria. Conversely, at 570 nm, no functional architecture could be seen in single-condition mode at any time ([Figures 4C and 4D](#);  $R = 0.21$  and  $R = 0.22$ ). Rather, large vascular activity patterns, unrelated to the functional columns, dominated the images. Analogous results were obtained in monkey V1 also upon imaging the orientation column system, with either full-field or small ( $0.75^\circ \times 1^\circ$ ) retinotopic stimulation.

The different hemodynamic processes should give rise to different, eventually orthogonal, spatio-temporal features in the image time series. We thus tried to reveal the hidden CBV changes in the parenchyma by decomposing the recorded time series of single-condition maps using principal component analysis (PCA). First, we applied PCA to the data recorded at 605 nm, where the processes contributing to the signal are known to have largely different spatio-temporal dynamics (the initial de-oxygenation phase as opposed to the delayed CBV and CBF response). The resulting eigenvectors could, in most experiments, be separated into a "mainly vascular" group and a "mainly functional" group, according to their similarity to the vascular patterns of the cortex or to the functional architecture, and noise. The eigenvectors were ordered according to the decreasing amplitude of their eigenvalues. For the single-condition maps shown in [Figure 2](#) and [Figure 3](#) (21 frames, 475 ms/frame), the 1<sup>st</sup> eigenvector displayed mostly vascular patterns ([Figure 4E](#);  $R = 0.05$ ). Summation of the eigenvectors displaying prevalently functional patterns (2<sup>nd</sup> to 4<sup>th</sup>) yielded the maps shown in [Figure 4F](#). This sum of "functional" eigenvectors clearly displayed the OD patterns, as identified by differential imaging in [Figure 1B](#) ( $R = 0.74$ ). The PCA of the time series of blood volume maps obtained at 570 nm yielded similar results. Summation of the eigenvectors displaying mostly vasculature (1<sup>st</sup> to 2<sup>nd</sup>) revealed the vascular patterns ( $R = 0.02$ ; [Figure 4G](#)), whereas summation of the eigenvectors displaying prevalently functional patterns (3<sup>rd</sup> to 5<sup>th</sup>) yielded a functional map, revealing the OD patterns ( $R = 0.41$ ; [Figure 4H](#)). The sum the eigenvalues until the 4<sup>th</sup> at 605 nm and the 5<sup>th</sup> at 570 nm represented ~97% and ~99%, respectively, of the whole spectrum. Visual inspection suggested that the remaining eigenvectors captured mainly nonphysiological noise. Indeed, inclusion of additional eigenvectors into either the vascular or the functional group introduced mainly shot-noise patterns into the images, without appreciably affecting either their vascular or functional patterns, nor their time course.

These results indicate that, when the large activation signals from the noncapillary vessels are successfully reduced, single-condition functional maps can be obtained also through activity-dependent CBV changes, even without introducing information from an orthogonal stimulus.

## Time Course and Relative Amplitudes of the Global and Mapping Components

[Figure 5A](#) shows the amplitudes of the vascular and functional components of single-condition maps obtained by PCA ([Figures 4E–4H](#)), as a function of time. To represent the time courses *specific* to the vascular component on one hand and to the functional component on the other, the temporal dynamics *common* both to the vasculature and to the parenchyma had been subtracted from the data before all PCA (see Experimental Procedures). For each wavelength, the time course of the vascular component strongly resembled that of the global signal, defined as the reflection change in single-condition maps averaged over the whole activated area ([Figure 5B](#)). The delay of the vascular component at 605 nm with respect to the global signal was expected, since oximetric changes specific to the macrovasculature (e.g., larger veins) occur later than in the microvasculature (capillary transit time  $\sim 2$  s). The time course of the functional component at 605 nm strongly resembled the mapping signal time course ([Figure 1D](#)), reflecting the local part of the oximetric signal, i.e., the monophasic time course of the [Hbr] gradient between active and nonactive columns ([Malonek and Grinvald, 1996](#)). The time course of the CBV functional component, however, displayed the quasilinear increase of the CBV mapping signal only at early ( $<3$  s) and late ( $>6$  s) times: due to its clear macrovascular elements, the 570 nm functional component ([Figure 4H](#)) captured also the macrovascular, global signal (the inverted polarity is due to the bright color of its vascular patterns), especially between  $\sim 3$  and 6 s, when the ratio of global versus mapping signal was largest.

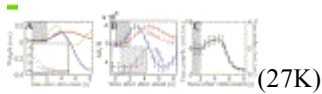


Figure 5. Weight of Vascular and Functional Components; Comparison of the Macrovascular Contribution to the Maps, Obtained at the Two Wavelengths(A) Time course of the weights of the vascular and functional patterns obtained by PCA (21 time frames, 475 ms/frame). Weights of vascular eigenvectors: 1<sup>st</sup> for 605 nm, blue; and 1<sup>st</sup> + 2<sup>nd</sup> for 570 nm, red. Weights of functional eigenvectors: 2<sup>nd</sup> + 3<sup>rd</sup> + 4<sup>th</sup> for 605 nm, yellow; and 3<sup>rd</sup> + 4<sup>th</sup> + 5<sup>th</sup> for 570 nm, green. For convenience, the 570 nm vascular time course (red) was downscaled by a factor of 10. Inset: first 20 eigenvalues, graphed semilogarithmically (basis 10). Blue: 605 nm, red: 570 nm.(B) Global signal: blue and red, 605 and 570 nm, respectively (red trace downscaled by a factor of 8). Inset: expanded view of the first 2 s of the response.(C) Time course of the ratio between the 570 and the 605 nm macrovascular signals, normalized by dividing it, for each point in time, by the mapping signal and corrected by multiplying by the surface density ratio of the activated vasculature at the two wavelengths (the uncorrected units appear on the right). Note that until  $\sim 1$  s after stimulus onset the ratio is meaningless, since both mapping and vascular signals have near-zero values. Error bars as in [Figure 1D](#).

[Figure 5B](#) shows the time course of the global signal. The downscaling factor used for the 570 nm signal was 8, twice that used for the mapping signal ([Figure 1D](#)), reflecting the smaller ratio of the local versus the global part of the intrinsic signal at 570 nm as compared to 605 nm. The same proportionality factor of  $\sim 2$  was found in analogous experiments performed in two other monkeys, whereas it was slightly smaller in the cat (1.7), probably due to effects of the anesthesia on the macrovasculature's response.

To further quantify the contribution of the nonlocal macrovascular component to the optical signals, we calculated the "vascular index" (Figure 5C, right-hand scale), a measure of the average macrovascular response, at 570 nm relative to 605 nm, scaled by the local component of the optical signals (see Experimental Procedures). To assess the effective contribution of the macrovascular response to the two-dimensional maps, the different spatial density of the activated vasculature seen at the two wavelengths was taken into account: the vascular contribution to the single-condition maps was 5–10 times stronger at 570 nm than at 605 nm for most of the time of activation, reaching a maximum of ~13 at ~4 s, and not decreasing below 2–4 even in the late part of the time course (Figure 5C, left-hand scale). This result shows that the macrovascular contribution in CBV single-condition maps is about one order of magnitude larger than for single-condition maps based on the oximetric signal during the initial dip, reflecting the weak localization of the overall CBV response to loci of electrical activity.

### Decomposition Procedure: Applicability

To be successful, the PCA decomposition requires the spatio-temporal response patterns of the macrovasculature, the capillaries, and the noise to be largely orthogonal. As expected, this is not always the case. Whereas the simple decomposition method used here was effective also in the orientation column system in area 18 of the anesthetized cat (Figure 6 and Figure 7), it was indeed only partially successful when applied to the orientation column system in area V1 of the awake monkey (Figure 8), which upon optical imaging yields functional maps characterized by a considerably lower SNR.

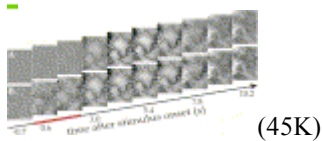


Figure 6. Time Development of Single-Condition Maps Obtained at 570 nm in Area 18 of the Anesthetized Cat with a 2 s Stimulus Consisting of a Drifting Horizontal Grating(A) To show the time development of the maps' amplitudes, the same clipping range of 1.5% was used for displaying every frame in the time series, after subtraction of its mean gray level. The slight brightening of the vasculature beginning at ~8 s is due to the onset of poststimulus oscillations (vasomotion noise), often observed at the end of the hemodynamic response, in particular in anesthetized preparations (e.g., Malonek et al., 1997). To enhance spatial patterns at each point in time, in (B), each frame was clipped individually to  $\pm 3$  standard deviations from its mean gray level. In both (A) and (B), the spatial pattern prior to stimulus onset was subtracted from all frames. Scale BAR = 1 mm. The red bar marks the time during which the stimulus was on.

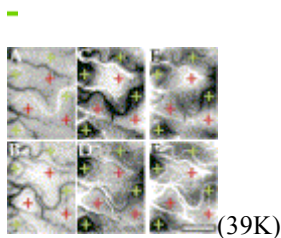


Figure 7. PCA Decomposition of Single Condition Orientation Maps in Area 18 of the Anesthetized Cat(A and B) Vascular component (C1) of the single-condition orientation maps obtained at 605 and 570 nm, respectively (clipping range: 2.0% and 1.3%).(C and D) Functional component (C2+C3) of the same maps,

taken at 605 and 570 nm, respectively (clipping range: 2.0% and 2.6%).(E and F) Differential maps, obtained dividing conditions stimulated with horizontal by conditions stimulated with vertical drifting gratings. (E) 605 nm, clipping range: 0.14%; (F) 570 nm, clipping range: 0.5%. Scale BAR = 1 mm.

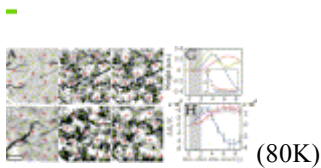


Figure 8. Decomposition of Single-Condition Orientation Maps in Awake Monkey V1(A and B) Vascular component (C1+C2) of the single condition orientation maps obtained at 605 and 570 nm, respectively (clipping range: 2.8% and 1.6%).(C and D) Functional component (C3+C4) of the same maps (clipping range: 0.5%).(E and F) Differential maps. (E) 605 nm, clipping range: 0.06%; (F) 570 nm, clipping range: 0.16%. Note that the oximetric (E) and CBV (F) maps are not identical (e.g., the black patch in [E] marked by a blue cross is shifted in [F]). Scale BAR = 0.5 mm.(G) Time course of the weights of the vascular (1<sup>st</sup> + 2<sup>nd</sup>: 605 nm, blue; 1<sup>st</sup> + 2<sup>nd</sup>: 570 nm, red) and functional (3<sup>rd</sup> + 4<sup>th</sup>: 605 nm, yellow; 3<sup>rd</sup> + 4<sup>th</sup>: 570 nm, green) eigenvectors obtained by PCA (23 time frames, 480 ms/frame). For convenience, the 570 nm vascular time course (red) was downscaled by a factor of 4. Inset: first 15 eigenvalues, graphed semilogarithmically (basis 10). Blue: 605 nm; red: 570 nm.(H) Global signal traces (left scale): blue and red, 605 and 570 nm (red trace downscaled by a factor of 8). Mapping signal (right scale): cyan and magenta, 605 and 570 nm (magenta trace downscaled by a factor of 4.2). Error bars: SEM of six independent experiments (plotted alternating between global and mapping signal for clarity of display).

[Figure 6](#) shows the time course of single-condition maps obtained at 570 nm in the anesthetized cat, using a 2 s stimulation paradigm with oriented square gratings. Again, the functional architecture was hidden by vascular activity.

However, when the single-condition maps were decomposed by PCA, vascular and functional patterns could be separated, and clear orientation patches were observed at both wavelengths, closely matching the functional maps obtained upon differential imaging ([Figure 7](#)). The time course of the functional and vascular components, as well as their relation to the mapping and global signals, was similar to those obtained in the OD system of the awake monkey. The eigenvalues corresponding to the eigenvectors included in the images of [Figures 7A–7D](#) accounted for 83% and 99% of the spectrum at 605 and 570 nm, respectively.

[Figures 8A–8D](#) shows the results of PCA applied to single-condition maps of the orientation system in V1 of a third monkey. At both wavelengths, a clear vascular component was obtained ([Figures 8A and 8B](#)) whose time course closely resembled that of the global signals ([Figures 8G and 8H](#)). The functional components ([Figures 8C and 8D](#)) allowed recovery of most of the patches identified by the differential maps ([Figures 8E and 8F](#)), and their weights' time courses resembled the corresponding mapping signals for the first ~3 s, like those obtained for the awake monkey ocular dominance system. The images were, however, strongly contaminated by vascular patterns. Furthermore, the eigenvalue spectrum decayed more slowly than for the OD maps ([Figure 8G](#), inset): the first four eigenvalues captured only 74% and 87% of the spectrum at 605 and 570 nm, respectively, indicating an only partially effective separation between vascular and functional eigenvectors and physiological noise. Indeed, the functional components

constructed from the 3<sup>rd</sup> and 4<sup>th</sup> eigenvectors ([Figures 8C and 8D](#)) less clearly reflected the functional architecture than in the previously described cases. Including additional eigenvectors increased the physiological (stimulus-unrelated) noise in the images more than it enhanced the functional patterns.

These results are most likely due to the lower amplitude of orientation maps as compared to OD maps in the monkey or to orientation maps in the cat, together with a similar physiological noise level. Indeed, on average the differential orientation maps in the monkey were characterized, respectively, at 605 and 570 nm by a 2.4 and 3.8 times smaller amplitude than the other differential maps shown here, whereas the amplitudes of the global signal were similar. Similar results have been obtained in numerous previous experiments performed in our laboratory using optical imaging of intrinsic signals.

## Discussion

### The Initial Dip and Prospects for High-Resolution Single-Condition Mapping with fMRI

[Malonek and Grinvald \(1996\)](#) suggested that restricting the fMRI acquisition to the highly localized early [Hbr] increase during the first ~4 s after stimulus onset could improve the spatial resolution. Indeed, intraoperative human studies combining various recording techniques ([Cannestra et al., 2001](#)) confirmed the higher localization of the initial dip as opposed to the positive BOLD. Furthermore, by focusing on the initial dip, [Kim et al. \(2000\)](#) and [Duong et al. \(2001\)](#) obtained high-resolution single-condition orientation maps in cats at 4.7 and 9.4 T. Recent direct oxygen measurements in the parenchyma have confirmed both the existence of the initial dip and its potential usefulness for functional imaging. Using oxygen electrodes, [Thompson et al. \(2003\)](#) showed that increases in neuronal spike rate were accompanied by immediate decreases in tissue oxygenation. Those could then be used to predict the functional properties of neighboring neurons. Since several independent methods have established a link between neural activity and microvascular deoxygenation, it appears that concerns raised by [Fransson et al. \(1998\)](#), [Buxton et al. \(1998\)](#), [Marota et al. \(1999\)](#), [Mandeville et al. \(1999\)](#), [Silva et al. \(2000\)](#), and [Lindauer et al. \(2001\)](#) were not warranted. However, blood oxygenation changes progress downstream from their origin in the capillary bed toward larger vessels within less than 2 s (capillary transit time). This restricts the time window for imaging related to electrical activity per se to less than 2 s, thus significantly limiting the achievable SNR. Although data from human subjects at field strengths up to 7 T suggest that the amplitude of the fMRI dip increases with the square of the field strength (depending to some extent also on the method of analysis) ([Ogawa et al. 1993](#) and [Yacoub and Hu 1999](#)), the practical feasibility of readily obtaining high-resolution maps based on the initial dip has thus remained an open issue ([Logothetis 2000](#) and [Kim 2000](#)). Nevertheless, we suggest that efforts in this direction would be rewarding, since oxygen extraction a priori colocalizes with electrical activity, yielding a hemodynamic signal that, at least in its early part (<2 s), is mainly passive from the point of view of the vasculature. In contrast, delayed activity-dependent CBV and CBF changes are an indirect result of electrical activity, mediated by the active vascular response. Since they certainly occur not only in small (<50  $\mu\text{m}$ ) but also in large vessels, they largely do not

colocalize with neuronal activity, raising the need for designing imaging procedures that selectively enhance the capillary signal.

### **Activity-Dependent CBV Changes Regulated at the Capillary Level Can Provide Columnar Resolution Single-Condition Functional Maps**

Previous optical imaging findings indicated that CBV, and thus also CBF, are inadequate for high-resolution single-condition mapping due to the large vascular response, which is uncorrelated with the functional architecture at the columnar level. Those include: poor oxy-hemoglobin maps found by imaging spectroscopy ([Malonek and Grinvald, 1996](#)), absence of single-condition maps in optical imaging studies performed at an isosbestic wavelength ([Vanzetta and Grinvald, 2001](#)), as well as the strong vascular response seen in late 605 nm single-condition maps ([Grinvald et al., 2000](#)). On the other hand, the spatial resolution may depend also on the cortical area. Using intrinsic optical imaging in auditory cortex, functional tonotopy could be mapped also at 540 nm ([Harel et al. 2000](#) and [Spitzer et al. 2001](#)), where the CBV signal dominates, and not only at oximetric wavelengths between ~610 and ~630 nm ([Bakin et al. 1996](#) and [Hess and Scheich 1996](#)). ([Spitzer et al. \[2001\]](#), however, failed to see tonotopic organization at 690 nm, a wavelength at which single-condition maps are readily obtained in visual cortex). Recently, [Sheth et al. \(2004\)](#) reported columnar resolution of CBV signals in rat somatosensory cortex, where, however, the layout of the microvasculature is known to correlate with the functional architecture. In the primate visual cortex, [Frostig et al. \(1990\)](#) showed that high-resolution (100–150  $\mu\text{m}$ ) differential maps, largely restricted to the cortical parenchyma, can be obtained by imaging CBV changes using optical imaging of intrinsic signals, as well as using an intravascular fluorescent contrast agent. These pioneering results clearly showed the existence of a capillary CBV component regulated at the columnar scale. Together with the results reported here, optical imaging studies thus support the notion of CBV and CBF regulation at the level of the capillaries, a concept that has often been denied.

Concerning functional brain mapping, here we obtained maps having the appearance of single-condition functional CBV maps by removing activity patterns originating from vessels down to ~50–100  $\mu\text{m}$ . Furthermore, we confirmed that these maps are indeed rather precise by comparing them with the well established gold standard for mapping OD and orientation columns. These results show that it is possible to obtain single-condition functional maps also through activity-dependent CBV changes, even without introducing information from an orthogonal stimulus, provided that the capillary component of the CBV response is selectively imaged. Most importantly, these conclusions are valid even though the postprocessing used here is not effective in the general case. In fact, they concern the spatio-temporal properties of the different physiological components of the hemodynamic signals per se and of the CBV response in particular. They are thus independent of whether the different components may or may not be successfully isolated by any particular decomposition method. Recently, Duong and colleagues found an elegant solution to this technical challenge. They obtained columnar resolution upon single-condition imaging with perfusion-based signals using the FAIR technique ([Duong et al., 2001](#)) and contrast agent-based fMRI (N. Harel et al., 2002, Neuroimage, abstract). With their MRI experimental protocols, the CBF or CBV

MRI signals could be enhanced in a rather selective way, appearing mostly in capillaries and being largely absent from larger vessels.

## Postprocessing versus Selective Data Acquisition

Upon PCA, the oximetric 605 nm signal originating from several spatio-temporally distinct hemodynamic processes (i.e., oxygen extraction and hyperoxygenation due to increase flow) separated into a global, nonlocal macrovascular component and a functional, local, mainly parenchymal component. This can probably be attributed to the characteristic spatio-temporal behavior of the oximetric signal, which colocalizes with loci of electrical activity mostly at the capillary level but much less so in other vessels. Such a separation occurred in some cases also for the PCA decomposition of the CBV response, being more effective the larger the SNR of the maps and the difference in time course between the mapping and the global signals. To be successful, in fact, the present PCA decomposition requires the spatio-temporal response patterns of the macrovasculature, the capillaries, and the noise to result in largely orthogonal processes. In other cases, other decomposition methods may yield better results. Several postprocessing procedures have been proposed in an attempt to reliably separate the functional signal from the global activation. Examples are PCA ([Sirovich and Everson 1992](#); [Sirovich et al. 1996](#) and [Cannestra et al. 1996](#)), indicator function ([Everson et al. 1997](#)), truncated difference approach ([Gabbay et al. 2000](#)), periodic stacking method ([Sornborger et al., 2003](#)), independent component analysis ([Bell and Sejnowski 1995](#) and [Hyvärinen and Oja 1997](#)), extended spatial decorrelation ([Molgedey and Schuster 1994](#); [Schiessl et al. 1999](#) and [Stetter et al. 2000](#)), introduction of weak temporal models ([Cheng-Bee et al. 1996](#) and [Zheng et al. 2001](#)), ANOVA-based statistical analysis ([Sheth et al., 2004](#)), and wavelets ([Carmona et al., 1995](#)). In spite of the progress made with respect to traditional differential or first frame analysis, however, the question of which method reliably performs better than the others across experimental designs, preparations, or even datasets acquired in different laboratories ([Zheng et al. 2001](#) and [Esposito et al. 2002](#)) appears to be still open. This underscores the difficulties inherent to the development of postprocessing procedures that succeed in the general case, in particular on data with low SNR.

Like most postprocessing methods, the simple PCA decomposition used here is not successful in the general case. It is thus not intended as a "cleaning procedure" for data containing large contributions from the macrovasculature. Still, the success of the PCA decomposition, even only in the particular case, proves the existence of a highly local capillary CBV response. This physiological result suggests that single-condition functional maps would be reliably obtained by selectively imaging the capillary component of the CBV/CBF response, *directly at the stage of data acquisition*, thus avoiding the shortcomings inherent to postprocessing procedures. Whereas upon optical imaging, such selective data acquisition is hampered by the surface vasculature that always contributes to the recorded signal, in fMRI, thin slices can be placed within the gray matter below the surface of the cortical sheet, avoiding the surface vessels' contributions. Using FAIR and contrast agent-based fMRI, [Duong et al. \(2001\)](#) and N. Harel et al. (2002, Neuroimage, abstract) obtained CBV and CBF responses containing

only small macrovascular contributions, suggesting that the technical goal of selectively imaging the capillary CBV or CBF response could be achieved by fMRI.

## **Prospects for fMRI using CBV or CBF Changes**

Our data indicate that a large part of the nonlocal CBV response originates from the macrovasculature, running tangentially to the cortical sheet: compared to the mapping signal, the macrovascular CBV signal is ~10 times larger than for oximetry-induced absorption changes, reflecting the much weaker colocalization of the CBV response with electrical activity than the [Hbr] increase during the initial dip. However, our data also suggest that single-condition maps can be obtained by using the CBV response, provided that the macrovascular component can be drastically reduced.

The three-dimensional vascular morphology of the various compartments of the cortical microcirculation suggests that high-resolution single-condition maps based on CBV or CBF responses can be obtained only if their source is limited to the capillaries, eventually considering also the velocity with which the hemodynamic signal propagates beyond the electrically active area. SNR considerations are obviously the most important criterion, and they vary from one methodology to the next. Thus, modeling that predicts the behavior of the various types of MRI signals, intrinsic or extrinsic, based on parameters that are derived from high spatial and temporal resolution optical imaging and electrical recordings would be fruitful. This is particularly true for oximetric, CBV, and CBF changes in capillaries, and shrinkage and expansion of the extracellular space ([Darquie et al., 2001](#)).

## **Experimental Procedures**

### **Preparation**

Experiments were performed on three adult male monkeys (*M. fascicularis*, 6–7 kg), with a transparent cranial window chronically implanted onto a  $\sim 2 \times 2$  cm aperture in the skull above the V1/V2 border, at about  $2.5^\circ$  eccentricity of the visual field. For a detailed description of all surgical and maintenance procedures, see [Shtoyerman et al. \(2000\)](#) and [Arieli et al. \(2002\)](#). Data from adult cat area 18 were acquired under sodium pentothal anesthesia. For details and surgical procedures see [Frostig et al. \(1990\)](#) and [Malonek et al. \(1997\)](#). All procedures were in accordance with NIH guidelines.

### **Experimental Paradigm**

The paradigm in the alert monkey experiments was a simple fixation task. A trial started when the monkey began fixation on a fixation point ( $0.08^\circ$ – $0.1^\circ$ ) displayed on a CRT screen. After a variable delay (2–3 s), a moving square grating appeared for 2 s, except in the blank conditions (no grating). The stimulus was then turned off, and the monkey had to continue to fixate until the fixation point disappeared, for a total fixation period varying between 11 and 12 s. Eye shutters were switched to ipsi- or contralateral stimulation. To allow for the relaxation of all hemodynamic signals, a dark-screen intertrial interval of  $\sim 10$  s followed. Data from trials where the monkey broke fixation were rejected. When imaging the orientation system in monkey V1, the paradigm was the

same, but the stimuli were binocular horizontal and vertical drifting gratings of optimal spatial and temporal frequency. In the anesthetized cat, we stimulated with drifting horizontal and vertical square gratings of optimal spatial and temporal frequency for area 18, moving for 2 s and separated by at least 20 s.

## Optical Imaging

Optical recordings were performed with a commercial imaging system (Imager 2001, Optical Imaging, Germantown, NY), adapted for the behaving monkey ([Shtoyerman et al., 2000](#)). The exposed cortex was illuminated (100 W tungsten halogen lamp, Zeiss, Germany) through interference filters (10 nm bandwidth; Omega Optical, Brattleboro, VT) and light guides. In the awake monkey, data were acquired in recording sessions of ~2 hr over several days. In each recording session, the wavelengths of 605 and 570 nm were interlaced at least once to avoid artifactual results due to drifts in the physiological state of the cortex, such a relatively slow alternation rate being sufficient, since the physiology is stable and so are the optical signals ([Shtoyerman et al., 2000](#)). In the anesthetized cat, where the physiology is less stable, wavelengths were interlaced every three stimuli by a computer-controlled filter wheel. To allow for a better identification of vascular activity patterns versus functional architecture, high magnification was used (13  $\mu\text{m}/\text{pixel}$ ), and the optical system was focused onto the cortical vasculature, rather than 300  $\mu\text{m}$  below the surface as traditionally done. Unless otherwise specified, image processing was always the same for both wavelengths (Gaussian high-pass filtering to eliminate very low spatial frequency gradients in the images: SIGMA = 650  $\mu\text{m}$ ). The amplitude of the displayed maps is given by the "clipping range." It specifies the range spanned by the employed grayscale in terms of fractional light intensity change with respect to the baseline.

## PCA and Time Course of the Macrovascular Signal

Time series of single-condition maps were decomposed into principal components after subtraction of the time course of the spatial mean, taken over the whole image (global signal). When possible, the resulting eigenvectors were classified as vascular, functional, and noise (a strategy similar to that used by [Stetter et al. \[2000\]](#) to reject the global part of the hemodynamic response and the vascular activity patterns from the optical signal), according to their similarity with the cortical vasculature or the functional patches obtained by differential imaging, respectively. Throughout the paper, "similarity" is quantified by R, the correlation coefficient with respect to the commonly used gold standard differential map obtained at 605 nm during the time window of the initial dip. To bias the sensitivity of the correlation coefficient toward the contribution of functional patterns over the contribution of the nonlocal vascular response, all the maps involved in the calculation were Gaussian low-pass filtered (sigma = 130  $\mu\text{m}$ ) before correlating them. Convolutions with Gaussians with sigma values between 65  $\mu\text{m}$  and 156  $\mu\text{m}$  yielded very similar results to those reported here: over this range, R changed by less than 0.05, first increasing up to sigma ~110  $\mu\text{m}$  and then decreasing, for all correlations performed between "physiological" maps. When correlating maps with random noise or with rotated maps, R increased nearly linearly with sigma, at a rate of 0.0002/ $\mu\text{m}$ . The ordering of the different values of R remained unchanged up to SIGMA = 400  $\mu\text{m}$ .

The eigenvectors coding for noise (physiological noise, shot-noise, dark noise) were rejected, and a vascular and a functional image were constructed by summing the eigenvectors in the respective groups. Vascular components were selected according to their correlation value with the image of the cortical vasculature. Functional components were chosen as components that exhibited a patchy appearance. The correlation coefficient is obviously sensitive to residual noise in the experimental data; a correlation value of 1 between two "identical" maps is never expected. To assess the significance of a given value of the correlation coefficient between two functional maps, the following information was thus obtained: (1) A value of  $R = 0.84$  was found for two identical differential maps, calculated from two independent datasets, obtained at 605 nm during the period of the initial dip. (2)  $|R|$  for correlation with filtered random noise was  $\sim 0.1$ . (3) As a "control" value,  $R$  calculated for two unrelated functional maps yielded  $-0.12$  (e.g., the differential map in [Figure 1B](#) was rotated by  $90^\circ$  and then correlated with itself). Thereafter, the weights in the single-condition time series of the vascular and the functional images as a function of time were calculated by projection (scalar product defined as pixel-by-pixel multiplication) of each frame in the single-condition time series onto the vascular and the functional images, respectively. For comparison to the weights of the vascular and functional images, the global signal was inverted ([Figure 5](#) and [Figure 8](#)), since it represents activation as a *decrease* in reflected light (whereas no inversion is needed for the mapping signal, which represents the difference in activation of functional patches between optimal and nonoptimal stimulation).

### **Vascular Index and Vascular Contribution**

The amplitude of the vascular contribution to the time series of the single-condition maps was calculated directly by averaging the signal over the macrovasculature (vessels  $>50 \mu\text{m}$ ) after subtraction of the mean time course (global signal). The activated blood vessels were selected from the single-condition map time series, and the time course was calculated separately for each wavelength (the activity patterns originating from the blood vessels were often different at 605 and 570 nm, since the two wavelengths enhance different hemodynamic processes). To obtain the effective weight of those vascular activity patterns with respect to the functional patterns, this vascular time course was normalized by the time course of the mapping signal, at each wavelength. The vascular index was then obtained by dividing this normalized time course at 570 by that obtained at 605 nm ([Figure 5C](#)). Next, we assessed the activated vessels' "surface density," defined by the number of activated vessels (independently of their color) crossed by a representative set of horizontal and vertical straight lines superimposed on the single-condition maps. The obtained surface density was 4–5 times larger at 570 than at 605 nm. Multiplication of the vascular index by the average surface density ratio of the activated vessels at the two wavelengths then yielded the "vascular contribution" to the maps ([Figure 5C](#)).

-

## **Acknowledgements**

We thank T. Eliahu, D. Eттner, Dr. D. Nelson, and E. Tzabari for technical assistance and Dr. G. Masson, S. Naaman, and D. Sharon for critical comments. This work was supported by grants from the Enoch, Goldsmith, and Glasberg and Korber Foundations, BMBF/MOS and ISF grants, and the Grodetsky Center (to A.G.).

-

## References

[Ances](#), B.M., Buerk, D.G., Greenberg, J.H. and Detre, J.A., 2001. Temporal dynamics of the partial pressure of brain tissue oxygen during functional forepaw stimulation in rats. *Neurosci. Lett.* **306**, pp. 106–110. [Abstract](#) | [Full Text + Links](#) | [PDF \(249 K\)](#)

[Arieli](#), A., Sterkin, A., Grinvald, A. and Aertsen, A., 1996. Dynamics of ongoing activity: explanation of the large variability in evoked cortical responses. *Science* **273**, pp. 1868–1871.

[Arieli](#), A., Grinvald, A. and Slovin, H., 2002. Dural substitute for long-term imaging of cortical activity in behaving monkeys and its clinical implications. *J. Neurosci. Methods* **114**, pp. 119–133. [Abstract](#) | [Full Text + Links](#) | [PDF \(547 K\)](#)

[Bakin](#), J.S., Kwon, M.C., Masino, S.A., Weinberger, N.M. and Frostig, R.D., 1996. Suprathreshold auditory cortex activation visualized by intrinsic signal optical imaging. *Cereb. Cortex* **6**, pp. 120–130.

[Bandettini](#), P.A., Wong, E.C., Hinks, R.S., Rikovsky, R.S. and Hyde, J.S., 1992. Time course EPI of human brain function during task activation. *Magn. Reson. Med.* **25**, pp. 390–397.

[Bell](#), A.J. and Sejnowski, T.J., 1995. An information-maximization approach to blind separation and blind deconvolution. *Neural Comput.* **7**, pp. 1129–1159.

[Bonhoeffer](#), T. and Grinvald, A., 1991. Iso-orientation domains in cat visual cortex are arranged in pinwheel-like patterns. *Nature* **353**, pp. 429–431.

[Bonhoeffer](#), T. and Grinvald, A., 1996. Optical imaging based on intrinsic signals: the methodology. In: Toga, A. and Mazziotta, J.C., Editors, 1996. *Brain Mapping: The Methods*, Academic Press, San Diego, CA, pp. 55–97.

[Bosking](#), W.H., Zhang, Y., Schofield, B. and Fitzpatrick, D., 1997. Orientation selectivity and the arrangement of horizontal connections in tree shrew striate cortex. *J. Neurosci.* **17**, pp. 2112–2127.

[Buxton](#), R.B., Wong, E.C. and Frank, L.R., 1998. Dynamics of blood flow and oxygenation changes during brain activation: the balloon model. *Magn. Reson. Med.* **39**, pp. 855–864.

[Cannestra](#), A.F., Blood, A.J., Black, K.L. and Toga, A.W., 1996. The evolution of optical signals in human and rodent cortex. *Neuroimage* **3**, pp. 202–208. [Abstract](#) | [PDF \(150 K\)](#)

[Cannestra](#), A.F., Pouratian, N., Bookheimer, S.Y., Martin, N.A., Becker, D.P. and Toga, A.W., 2001. Temporal spatial differences observed by functional MRI and human intraoperative optical imaging. *Cereb. Cortex* **11**, pp. 773–782.

[Carmona](#), R.A., Hwang, W.L. and Frostig, R.D., 1995. Wavelet analysis for brain-function imaging. *IEEE Trans. Med. Imaging* **14**, pp. 556–564.

[Cheng-Bee](#), C.H., Kwon, M.C., Masino, S.A. and Frostig, R.D., 1996. Areal extent quantification of functional representations using intrinsic signal optical imaging. *J. Neurosci. Methods* **68**, pp. 27–37.

[Cheng](#), K., Waggoner, R.A. and Tanaka, K., 2001. Human ocular dominance columns as revealed by high-field functional magnetic resonance imaging. *Neuron* **32**, pp. 359–374. [SummaryPlus](#) | [Full Text + Links](#) | [PDF \(1495 K\)](#)

[Darquie](#), A., Poline, J.-B., Poupon, C., Saint-Jalmes, H. and Le Bihan, D., 2001. Transient decrease in water diffusion observed in human occipital cortex during visual stimulation. *Proc. Natl. Acad. Sci. USA* **98**, pp. 9391–9395.

[Duong](#), T.Q., Kim, D.-S., Ugurbil, K. and Kim, S.-G., 2001. Localized cerebral blood flow response at submillimeter columnar resolution. *Proc. Natl. Acad. Sci. USA* **98**, pp. 10904–10909.

[Ernst](#), T. and Hennig, J., 1994. Observation of a fast response in functional MR. *Magn. Reson. Med.* **32**, pp. 146–149.

[Esposito](#), F., Formisano, E., Seifritz, E., Goebel, R., Morrone, R., Tedeschi, G. and Di Salle, F., 2002. Spatial independent component analysis of functional MRI time-series: to what extent do results depend on the algorithm used?. *Hum. Brain Mapp.* **16**, pp. 146–157.

[Everson](#), R.M., Knight, B.W. and Sirovich, L., 1997. Separating spatially distributed response to stimulation from background. I. Optical Imaging. *Biol. Cybern.* **77**, pp. 407–417.

[Fox](#), P.T. and Raichle, M.E., 1985. Stimulus rate determines regional brain blood flow in striate cortex. *Ann. Neurol.* **17**, pp. 303–305.

[Fransson](#), P., Kruger, G., Merboldt, K.D. and Frahm, J., 1998. Temporal characteristics of oxygenation-sensitive MRI responses to visual activation in humans. *Magn. Reson. Med.* **39**, pp. 912–919.

[Frostig](#), R.D., Lieke, E.E., Ts'o, D.Y. and Grinvald, A., 1990. Cortical functional architecture and local coupling between neuronal activity and the microcirculation revealed by in vivo high-resolution optical imaging of intrinsic signals. *Proc. Natl. Acad. Sci. USA* **87**, pp. 6082–6086.

[Gabbay](#), M., Brennan, C., Kaplan, E. and Sirovich, L., 2000. A principal components-based method for the detection of neuronal activity maps: application to optical imaging. *Neuroimage* **11**, pp. 313–325. [Abstract](#) | [Abstract + References](#) | [PDF \(273 K\)](#)

- [Goodyear](#), B.G. and Menon, R.S., 2001. Brief visual stimulation allows mapping of ocular dominance in visual cortex using fMRI. *Hum. Brain Mapp.* **14**, pp. 210–217.
- [Grinvald](#), A., Lieke, E., Frostig, R.D., Gilbert, C.D. and Wiesel, T.N., 1986. Functional architecture of cortex revealed by optical imaging of intrinsic signals. *Nature* **324**, pp. 361–364.
- [Grinvald](#), A., Sloviter, H. and Vanzetta, I., 2000. Non-invasive visualization of cortical columns by f-MRI. *Nat. Neurosci.* **3**, pp. 105–107.
- [Harel](#), N., Mori, N., Sawada, S., Mount, R.J. and Harrison, R.V., 2000. Three distinct auditory areas of cortex (AI, AII, and AAF) defined by optical imaging of intrinsic signals. *Neuroimage* **11**, pp. 302–312. [Abstract](#) | [Abstract + References](#) | [PDF \(852 K\)](#)
- [Hess](#), A. and Scheich, H., 1996. Optical and FDG mapping of frequency specific activity in auditory cortex. *Neuroreport* **7**, pp. 2643–2647.
- [Hu](#), X., Le, T.H. and Ugurbil, K., 1997. Evaluation of the early response in fMRI in individual subjects using short stimulus duration. *Magn. Reson. Med.* **37**, pp. 877–884.
- [Hyvärinen](#), A. and Oja, E., 1997. A fast fixed point algorithm for independent component analysis. *Neural Comput.* **9**, pp. 1483–1492.
- [Kim](#), D.-S., 2000. Can current fMRI techniques reveal the micro-architecture of cortex. *Nat. Neurosci.* **3**, p. 414.
- [Kim](#), D.-S., Doung, T.Q. and Kim, S.-G., 2000. High-resolution mapping of iso-orientation columns by fMRI. *Nat. Neurosci.* **3**, pp. 164–199.
- [Kwong](#), K.K., Belliveau, J.W., Chesler, D.A., Goldberg, I.E., Weisskoff, R.M., Poncelet, B.P., Kennedy, D.N., Hoppel, B.E., Cohen, M.S., Turner, R. *et al.*, 1992. Dynamic magnetic resonance imaging of human brain activity during primary sensory stimulation. *Proc. Natl. Acad. Sci. USA* **89**, pp. 5675–5679.
- [Lindauer](#), U., Royle, G., Leithner, C., Köhl, M., Gold, L., Gethmann, J., Kohl-Bareis, M., Villringer, A. and Dirnagl, U., 2001. No evidence for early decrease in blood oxygenation in rat whisker cortex in response to functional activation. *Neuroimage* **13**, pp. 988–1001. [Abstract](#) | [Abstract + References](#) | [PDF \(490 K\)](#)
- [Logothetis](#), N.K., 2000. Can current fMRI techniques reveal the micro-architecture of cortex. *Nat. Neurosci.* **3**, pp. 413–414.
- [Logothetis](#), N.K., Guggenberger, H., Peled, S. and Pauls, J., 1999. Functional imaging of the monkey brain. *Nat. Neurosci.* **2**, pp. 555–562.
- [Malonek](#), D. and Grinvald, A., 1996. Interactions between electrical activity and cortical microcirculation revealed by imaging spectroscopy: implications for functional brain mapping. *Science* **272**, pp. 551–554.

- [Malonek](#), D., Dirnagl, U., Lindauer, U., Yamada, K., Kanno, I. and Grinvald, A., 1997. Vascular imprints of neuronal activity: relationships between the dynamics of cortical blood flow, oxygenation, and volume changes following sensory stimulation. *Proc. Natl. Acad. Sci. USA* **94**, pp. 14826–14831.
- [Mandeville](#), J.B., Marota, J.J., Ayata, C., Moskowitz, M.A., Weisskoff, R.M. and Rosen, B.R., 1999. MRI measurement of the temporal evolution of relative CMRO(2) during rat forepaw stimulation. *Magn. Reson. Med.* **42**, pp. 944–951.
- [Marota](#), J.J., Ayata, C., Moskowitz, M.A., Weisskoff, R.M., Rosen, B.R. and Mandeville, J.B., 1999. Investigation of the early response to rat forepaw stimulation. *Magn. Reson. Med.* **41**, pp. 247–252.
- [Martin](#), C., Berwick, J., Johnston, D., Zheng, Y., Martindale, J., Port, M., Redgrave, P. and Mayhew, J., 2002. Optical imaging spectroscopy in the unanaesthetised rat. *J. Neurosci. Methods* **120**, pp. 25–34. [Abstract](#) | [Full Text + Links](#) | [PDF \(659 K\)](#)
- [Masino](#), S.A., 2003. Quantitative comparison between functional imaging and single-unit spiking in rat somatosensory cortex. *J. Neurophysiol.* **89**, pp. 1702–1712.
- [Mayhew](#), J., Zheng, Y., Hou, Y., Vuksanovic, B., Berwick, J., Askew, S. and Coffey, P., 1999. Spectroscopic analysis of changes in remitted illumination: the response to increased neural activity in brain. *Neuroimage* **10**, pp. 304–326. [Abstract](#) | [Abstract + References](#) | [PDF \(852 K\)](#)
- [Menon](#), R.S., Ogawa, S., Hu, X., Strupp, J.P., Anderson, P. and Ugurbil, K., 1995. BOLD based functional MRI at 4 Tesla includes a capillary bed contribution: echo-planar imaging correlates with previous optical imaging using intrinsic signals. *Magn. Reson. Med.* **33**, pp. 453–459.
- [Menon](#), R.S., Ogawa, S., Strupp, J.P. and Ugurbil, K., 1997. Ocular dominance in human V1 demonstrated by functional magnetic resonance imaging. *J. Neurophysiol.* **77**, pp. 2780–2787.
- [Molgedey](#), L. and Schuster, H.G., 1994. Separation of a mixture of independent signals using time delayed correlations. *Phys. Rev. Lett.* **72**, pp. 3634–3637.
- [Ogawa](#), S., Lee, T.M., Kay, A.R. and Tank, D.W., 1990. Brain magnetic resonance imaging with contrast dependent on blood oxygenation. *Proc. Natl. Acad. Sci. USA* **87**, pp. 9868–9872.
- [Ogawa](#), S., Tank, D.W., Menon, R., Ellermann, J.M., Kim, S.-G., Merkle, H. and Ugurbil, K., 1992. Intrinsic signal changes accompanying sensory stimulation: functional brain mapping with magnetic resonance imaging. *Proc. Natl. Acad. Sci. USA* **89**, pp. 5951–5955.
- [Ogawa](#), S., Menon, R., Tank, D.W., Kim, S.-G., Merkle, H., Ellermann, J.M. and Ugurbil, K., 1993. Functional brain mapping by blood oxygenation level-dependent

contrast magnetic resonance imaging. A comparison of signal characteristics with a biophysical model. *Biophys. J.* **64**, pp. 803–812.

[Roy](#), C. and Sherrington, C., 1890. On the regulation of the blood supply of the brain. *J. Physiol.* **11**, pp. 85–108.

[Schiessl](#), I., Stetter, M., Mayhew, J.E.W., Askew, A., McLoughlin, N., Levitt, J.B., Lund, J.S., and Obermayer, K. (1999). Blind separation of spatial signal patterns from optical imaging records. In Proceedings of the First International Workshop on Independent Component Analysis and Blind Signal Separation, Aussois, France, Volume 1, J.-F. Cardoso, C. Jutten, and P. Loubaton, eds. pp. 179–184.

[Sheth](#), S.A., Nemoto, M., Guiou, M., Walker, M., Pouratian, N., Hageman, N. and Toga, A.W., 2004. Columnar specificity of microvascular oxygenation and volume responses: implications for functional brain mapping. *J. Neurosci.* **24**, pp. 634–641.

[Shmuel](#), A. and Grinvald, A., 1996. Functional organization for direction of motion and its relationship to orientation maps in cat area 18. *J. Neurosci.* **16**, pp. 6945–6964.

[Shoham](#), D. and Grinvald, A., 2001. The cortical representation of the hand in macaque and human area S-I: high resolution optical imaging. *J. Neurosci.* **21**, pp. 6820–6835.

[Shoham](#), D., Hubener, M., Schulze, S., Grinvald, A. and Bonhoeffer, T., 1997. Spatio-temporal frequency domains and their relation to cytochrome oxidase staining in cat visual cortex. *Nature* **385**, pp. 529–533.

[Shtoyerman](#), E., Arieli, A., Slovin, H., Vanzetta, I. and Grinvald, A., 2000. Long-term optical imaging and spectroscopy reveal mechanisms underlying the intrinsic signal and stability of cortical maps in V1 of behaving monkeys. *J. Neurosci.* **20**, pp. 8111–8121.

[Silva](#), A.C., Lee, S.P., Iadecola, C. and Kim, S.G., 2000. Early temporal characteristics of cerebral blood flow and deoxyhemoglobin changes during somatosensory stimulation. *J. Cereb. Blood Flow Metab.* **20**, pp. 201–206.

[Sirovich](#), L. and Everson, R.M., 1992. Management and analysis of large scientific datasets. *Int. J. Supercomputer Applications* **6**, pp. 50–68.

[Sirovich](#), L., Everson, R.M., Kaplan, E., Knight, B.W., O'Brien, E.V. and Orbach, D., 1996. Modeling the functional organization of the visual cortex. *Physica D.* **96**, pp. 355–366. [Abstract](#) | [Abstract + References](#) | [PDF \(721 K\)](#)

[Sornborger](#), A., Sailstad, C., Kaplan, E. and Sirovich, L., 2003. Spatiotemporal analysis of optical imaging data. *Neuroimage* **18**, pp. 610–621. [Abstract](#) | [PDF \(621 K\)](#)

[Spitzer](#), M.W., Calford, M.B., Clarey, J.C., Pettigrew, J.D. and Roe, A.W., 2001. Spontaneous and stimulus-evoked intrinsic optical signals in primary auditory cortex of the cat. *J. Neurophysiol.* **85**, pp. 1283–1298.

[Stetter](#), M., Schiessl, I., Otto, T., Sengpiel, F., Hubener, M., Bonhoeffer, T. and Obermayer, K., 2000. Principal component analysis and blind separation of sources for

optical imaging of intrinsic signals. *Neuroimage* **5**, pp. 482–490. [Abstract](#) | [Abstract + References](#) | [PDF \(565 K\)](#)

[Thompson](#), J.K., Peterson, M.R. and Freeman, R.D., 2003. Single-neuron activity and tissue oxygenation in the cerebral cortex. *Science* **299**, pp. 1070–1072.

[Vanzetta](#), I. and Grinvald, A., 1999. Increased cortical oxidative metabolism due to sensory stimulation: implications for functional brain imaging. *Science* **286**, pp. 1555–1558.

[Vanzetta](#), I. and Grinvald, A., 2001. Evidence and lack of evidence for the initial dip in the anesthetized rat: implications for human functional brain imaging. *Neuroimage* **13**, pp. 959–967. [Abstract](#) | [Abstract + References](#) | [PDF \(957 K\)](#)


[Wang](#), G., Tanaka, K. and Tanifuji, M., 1996. Optical imaging of functional organization in the monkey inferotemporal cortex. *Science* **272**, pp. 1665–1668.

[Weliky](#), M., Bosking, W.H. and Fitzpatrick, D., 1996. A systematic map of direction preference in primary visual cortex. *Nature* **379**, pp. 725–728.

[Yacoub](#), E. and Hu, X., 1999. Detection of the early negative response in fMRI at 1.5 Tesla. *Magn. Reson. Med.* **41**, pp. 1088–1092.

[Zheng](#), Y., Johnston, D., Berwick, J. and Mayhew, J., 2001. Signal source separation in the analysis of neural activity in brain. *Neuroimage* **13**, pp. 447–458. [Abstract](#) | [Abstract + References](#) | [PDF \(644 K\)](#)

-

 Corresponding author. Correspondence: Ivo Vanzetta, +33 (0)491 164582 (phone), +33 (0)491 774969 (fax)

<sup>1</sup> Present address: Equipe Dynamique de la Vision et de l'Action INCM, CNRS-UMR 6193 (Bat. N'), 31 Chemin Joseph Aiguier, 13402 Marseille Cedex 20, France.